nature materials

ARTICLES

https://doi.org/10.1038/s41563-019-0488-z

Nanoscale semiconductor/catalyst interfaces in photoelectrochemistry

Forrest A. L. Laskowski, Sebastian Z. Oener, Michael R. Nellist, Adrian M. Gordon, David C. Bain, Jessica L. Fehrs and Shannon W. Boettcher*

Semiconductor structures (for example, films, wires, particles) used in photoelectrochemical devices are often decorated with nanoparticles that catalyse fuel-forming reactions, including water oxidation, hydrogen evolution or carbon-dioxide reduction. For high performance, the catalyst nanoparticles must form charge-carrier-selective contacts with the underlying light-absorbing semiconductor, facilitating either hole or electron transfer while inhibiting collection of the opposite carrier. Despite the key role played by such selective contacts in photoelectrochemical energy conversion and storage, the underlying nanoscale interfaces are poorly understood because direct measurement of their properties is challenging, especially under operating conditions. Using an n-Si/Ni photoanode model system and potential-sensing atomic force microscopy, we measure interfacial electron-transfer processes and map the photovoltage generated during photoelectrochemical oxygen evolution at nanoscopic semiconductor/catalyst interfaces. We discover interfaces where the selectivity of low-Schottky-barrier n-Si/Ni contacts for holes is enhanced via a nanoscale size-dependent pinch-off effect produced when surrounding high-barrier regions develop during device operation. These results thus demonstrate (1) the ability to make nanoscale operando measurements of contact properties under practical photoelectrochemical conditions and (2) a design principle to control the flow of electrons and holes across semiconductor/catalyst junctions that is broadly relevant to different photoelectrochemical devices.

Nanoscale interfaces play a central role in devices used for photoelectrochemical energy conversion and storage. Catalyst nanoparticles are often sparsely deposited onto photoactive semiconductors such that they selectively collect either electrons or holes, drive fuel-forming reactions at low overpotentials and minimally block incoming light[1]. The properties of the resulting semiconductor/catalyst nanojunctions are probably heterogeneous and vary substantially based on surface treatment, deposition method, particle size or electrochemical conditioning[2,3]. Additionally, heterogeneous nanoscale interfaces can be formed during device operation from initially homogeneous interfaces. For example, Ni catalyst films on n-Si photoanodes are thought to transform into isolated nanojunctions during photoelectrochemical operation[4,5]. Heterogeneous semiconductor/catalyst interfaces are difficult to characterize electrically, especially at the nanoscale resolution required under relevant photoelectrochemical conditions. While the properties of uniform planar semiconductor/metal interfaces (Schottky contacts) have been studied in detail and provide a valuable reference[6], major changes in interfacial electrical behaviour occur as the contact dimensions approach or become less than the semiconductor depletion width (~10–1,000 nm)[7].

Techniques have been developed for mapping heterogeneous interfacial properties in photovoltaic and (photo)electrochemical systems. Nanoscale open-circuit-voltage mapping of solid-state photovoltaics is possible via Kelvin-probe force microscopy (KPFM)[8]. The application of KPFM, or related electrochemical-force microscopies[9], to (photo)electrochemical systems is challenged by the presence of practical electrolyte concentrations[10]. Photoconductive atomic force microscopy (AFM) was used to illustrate heterogeneous electrical transport properties in semiconductor photoelectrodes[11], but the measurements were performed ex situ and details of how nanoscale electrocatalysts interface with the semiconductor remain unexplored. Scanning electrochemical microscopy (SECM)[12] and scanning electrochemical cell microscopy[13] can map catalytic reaction rates by monitoring product formation, but do not directly provide information on the electrical properties of underlying semiconductor/catalyst interfaces. Scanning electrochemical potential microscopy can be used either to measure potential gradients through electrical double layers or to map constant-potential surfaces. However, it is challenging to map nonconstant surface potentials in many experimental systems because the measurement conflates potential with topography[14,15]. Recently, we developed a potential-sensing electrochemical AFM (PS-EC-AFM) technique to measure the surface potential of continuous metal-oxyhydroxide catalyst films on metal-oxide photoelectrodes, showing how the oxyhydroxides behaved as both hole-collecting layers and catalysts for water oxidation[4,16].

Here we use PS-EC-AFM to spatially resolve the interfacial electronic properties of nanoscale semiconductor/catalyst interfaces. As a model system, we study nominally hemispherical Ni nanocontacts electrodeposited onto n-Si, following ref. [17]. The n-Si/Ni interface has been studied extensively as a 'stabilized' photoanode for water oxidation under neutral-to-basic conditions[4,5,18–20]. Generally n-Si photoelectrodes with thinner Ni films or smaller Ni nanoparticles perform better (following electrochemical conditioning) than those with higher Ni loading[19,20]. Here we find that electrodeposition of Ni nanoparticles on n-Si leads to low-Schottky-barrier (~0.61 V) contacts, which under dry conditions yield photovoltages of only ~300 mV, independent of Ni nanoparticle size. Following photoelectrochemical potential cycling, the surfaces of the Ni nanocontacts convert to nickel (oxy)hydroxide (that is, $Ni(OH)_2$ or NiOOH). Further ex situ electrical measurements of the semiconductor/catalyst junction are not possible because the catalyst resting state, $Ni(OH)_2$, is electrically insulating. During photoelectrochemical oxygen evolution, $Ni(OH)_2$ is oxidized to electrically conducting NiOOH. Operando photovoltages measured on individual

Department of Chemistry and Biochemistry, University of Oregon, Eugene, OR, USA. *e-mail: swb@uoregon.edu

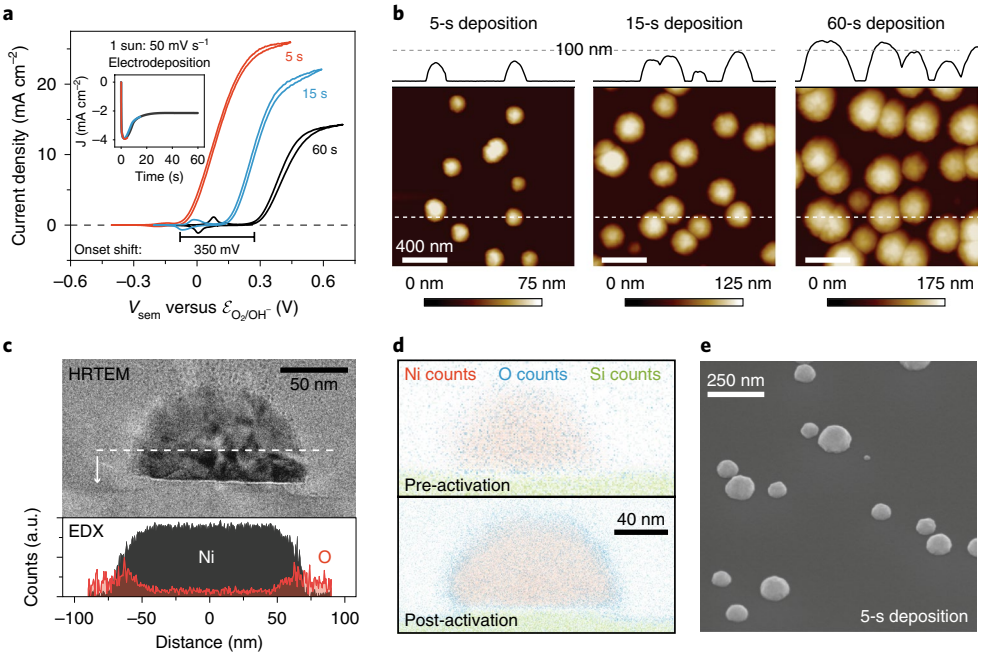

Fig. 1 | Characteristics of photoanodes fabricated by electrodeposition of Ni nanoislands onto n-Si. a, Photoelectrochemical data for n-Si/Ni collected at 50 mV s^{-1} in aqueous 1 M KOH under 100 mW cm^{-2} AM1.5G illumination (1 sun) following 50 CV cycles to activate the photoelectrode. V_{sem} is the potential applied to the semiconductor ohmic contact. The photocurrent onset, defined at 1 mA cm^{-2}, is improved by ~350 mV for 5-s Ni deposition relative to 60 s. The inset depicts characteristic chronoamperometry data for 5-, 15- and 60-s of deposition. **b**, AFM data collected immediately after 5-, 15- and 60-s depositions, with height line scans shown above each image. The results are characteristic of each specific surface, although regions of larger/smaller islands can sometimes be found. For the 5-s deposition, the Ni-island radius was 35–150 nm. **c**, High-resolution TEM (HRTEM) images and the associated energy-dispersive X-ray (EDX) analysis data show that activation of the n-Si/Ni photoelectrode converts the Ni surface to $Ni(OH)_2$/NiOOH (a.u., arbitrary units). **d**, Energy-dispersive X-ray composition maps before (top) and after (bottom) photoanodic activation of n-Si with 5-s Ni deposition. The maps illustrate the conversion of Ni to $Ni(OH)_2$/NiOOH. Additional elemental maps for nonactivated and activated islands can be found in Supplementary Section 1. **e**, SEM image (at 45°) characteristic of 5-s Ni deposition.

nanoscale n-Si/Ni/NiOOH junctions by PS-EC-AFM dramatically increase with cycling and show a strong dependence on nanocontact size. We explain the size dependence quantitatively by the 'pinch-off' effect[7,21,22], where the oxidized (high work function) NiOOH induces a large depletion region surrounding the n-Si/Ni interface during operation that increases the effective n-Si/Ni interface barrier and enhances the interfacial selectivity for holes[19,20,23]. Here 'selectivity' is defined as the interface's ability to collect minority carriers over majority carriers (that is, the ratio of the minority-carrier exchange current to majority-carrier exchange current)[24]. This finding not only demonstrates a direct nanoscale measurement of the pinch-off effect in a photoelectrochemical system[25], but also illustrates a potentially useful contact behaviour where selectivity is enhanced, during operation, by oxidation of an electrochemically active surrounding region. Such pinch-off or surface-gating effects are relevant to any semiconductor-based solar-energy-conversion device involving nanoscale elements[26].

Photoelectrochemistry of n-Si with Ni nanoislands

The photoelectrochemical behaviour of semiconductor photoanodes is typically dependent on the amount of catalyst deposited. We study n-Si photoanodes (dopant density 5–8 × 10^{15} cm^{-3}) onto which Ni metal islands have been deposited from 0.01 M $NiCl_2$ in aqueous 0.1 M H_3BO_3 at −1.5 V versus Ag/AgCl for 5, 15 or 60 s. The photoelectrochemical response of these photoanodes, after 50 cyclic voltammogram (CV) sweeps in aqueous 1 M KOH under ~1 sun illumination, is shown in Fig. 1a. This photoelectrochemical activation converts the outer portion of the Ni to $Ni(OH)_2$/NiOOH. Iron impurities that catalyse the oxygen evolution reaction (OER) are incorporated from the electrolyte and are assumed to be present in all catalysts studied[27]. Formation of the Ni (oxy) hydroxide is apparent from the increasing size of the Ni redox wave at potentials negative of the photocurrent onset (Fig. 1a) and from cross-sectional transmission electron microscopy (TEM; Fig. 1b and Supplementary Section 1). Samples prepared with 5-s deposition produced photoanodes with the most-negative photocurrent-onset potentials (that is, the highest photoanode performance) and spatially distributed Ni nanoislands with radii ranging from 35–150 nm (Fig. 1b,c). The 15- and 60-s depositions produced successively larger Ni islands (Fig. 1c). The thicker Ni led to more-positive photocurrent-onset potentials as well as lower photocurrents due to parasitic light absorption.

Schottky barrier heights at individual n-Si/Ni nanocontacts were measured ex situ (that is, in air) via conductive AFM before photoelectrochemical activation. A representative area was topographically imaged, single Ni nanocontacts were brought into contact with the conductive AFM tip (0.5-V piezo-deflection voltage) and dark J–V curves were collected (Fig. 2a, inset). The barrier height, ϕ_b, was calculated from exchange-current densities, $J_0 = A^* T^2 \left(e^{-q\phi_b/kT}\right)$, where A^* is the effective Richardson constant, T is the temperature, q is the elementary charge and k is the Boltzmann constant, by extrapolating the linear forward-bias region of the dark ln $|J|$–V curves to the y-intercept (ideality factors can be found in Supplementary Section 2). The fits show that the barrier height is independent of Ni island size (Fig. 2a), with a value (0.61 ± 0.01 V) near that of bulk n-Si/Ni contacts (~0.58 V)[28].

The illuminated V_{oc} of each nanocontact was measured under ~5-sun-equivalent flux using a 690-nm laser contained in the

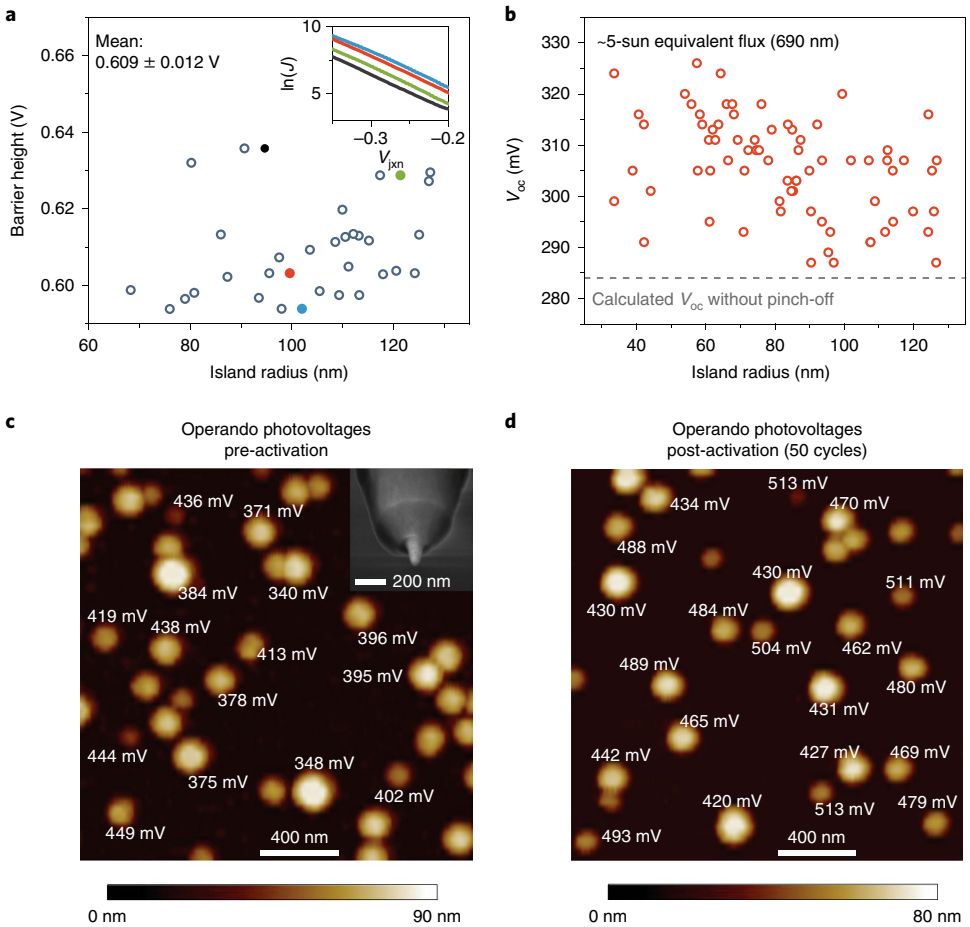

Fig. 2 | Characterization of n-Si/Ni photoelectrodes obtained from 5-s deposition. a, n-Si/Ni barrier heights collected ex situ from electrodes without activation show no dependence on Ni nanocontact radius. The inset shows ln|*J*|–*V* curves for the four coloured points, where V_{jxn} is the potential applied across the n-Si/Ni-island junction. **b**, Open circuit potential (V_{oc}) measurements extracted ex situ, under ~5-sun-effective illumination (690 nm), from electrodes without activation also show no significant dependence on Ni-nanocontact radius. **c**, Operando photovoltages collected using PS-EC-AFM before extended electrochemical activation, by landing the AFM tip on individual nanocontacts. The inset shows an SEM image of the PS-EC-AFM Pt nanoelectrode tip. **d**, Operando photovoltages collected at a different location after cycling the electrode under illumination from −0.35 to 0.35 V versus $\mathcal{E}_{O_2/OH^-}$ 50 times.

AFM unit (Supplementary Section 3). The V_{oc} values of 310 ± 10 mV show little dependence on island size and agree with the calculated V_{oc} of 284 mV for a 0.61-V n-Si/Ni Schottky barrier under experimental illumination (Fig. 2b). These barrier-height and V_{oc} results indicate that size-dependent interface behaviour is not present for the as-deposited nanocontacts and thus cannot, per se, explain the photocurrent-onset-potential differences with Ni deposition time (Fig. 1a).

We next studied the nanocontacts under photoelectrochemical conditions. Conductive AFM cantilevers, in which the entire tip was isolated from the solution by a dielectric layer except for the apex, were used (inset in Fig. 2c)[29]. The custom AFM photoelectrochemistry cell and measurement details are discussed in Supplementary Section 2. Under illumination, the semiconductor back-ohmic contact was biased at a potential such that the catalyst particles were held in the electrically conductive NiOOH state while few bubbles were produced (that is, near the photocurrent-onset potential; vigorous bubble generation interferes with the AFM measurement). The surface was then topographically imaged and the photovoltage—that is, the difference between the measured AFM tip potential and the potential applied to the semiconductor ohmic contact ($V_{ph} = V_{tip} - V_{sem}$)—was measured individually on each island. Photovoltages were collected both before and after activation with 50 photoanodic CV cycles (Fig. 2c,d); this activation was used because, even for the smallest islands, most of the original metallic Ni remains and the nanoislands retain a nominally hemispherical shape. Notably, the photovoltages are not only substantially higher (in some cases, >500 mV) than those measured under dry ex situ conditions, but they are also dependent on contact area (taken to be the two-dimensional geometric area in the AFM topography image) and increase with activation time. These results indicate a size-dependent mechanism for increasing the Ni-nanocontact carrier selectivity that is operative only in the presence of the OER-active NiOOH surface layer.

Analytical model for pinch-off at nanocontacts

The experimentally observed size-dependent photovoltage can be explained by the pinch-off effect[22], which occurs when an interface has spatially heterogeneous electrostatic barrier heights with low-barrier patches (here ϕ_b^{Ni}) surrounded by a higher-barrier background ϕ_b^0 (Fig. 3a). Pinch-off occurs when the depletion region induced by the adjacent higher-barrier region overlaps with the patch's depletion region (that is, with decreasing contact size the contact's selectivity is increasingly dominated by the work function

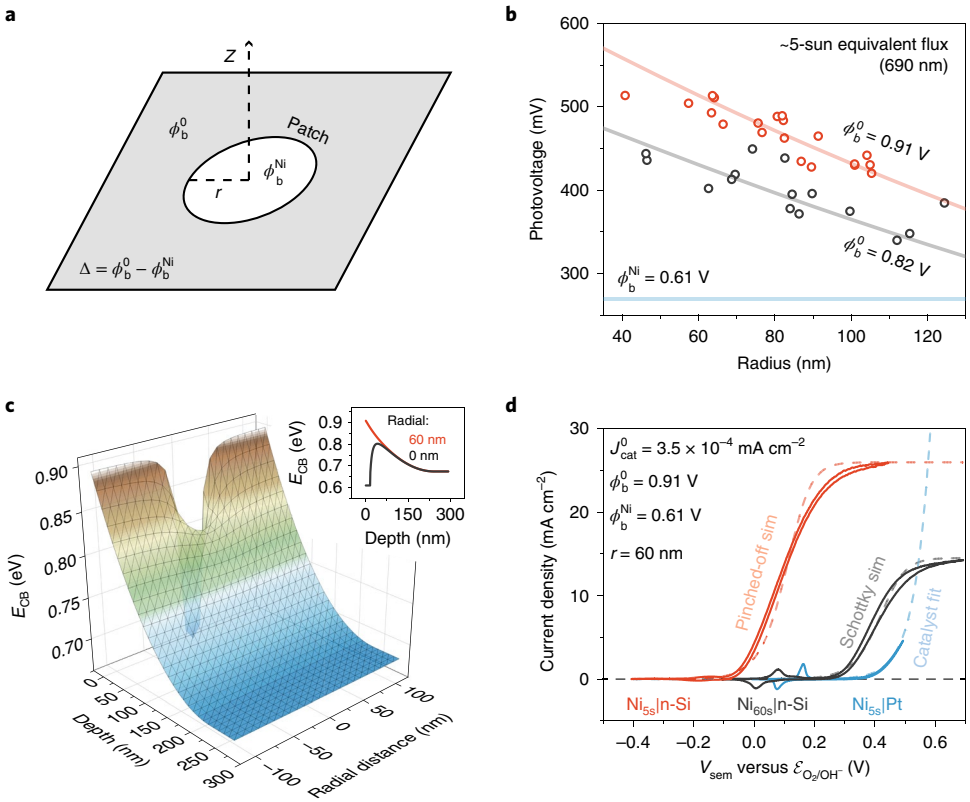

Fig. 3 | Simulations showing how the pinch-off model explains performance enhancements with catalyst nanocontacts. a, Tung's model[30] for a circular patch geometry is used where a small barrier $\phi_b^{Ni} = 0.61$ V representing the n-Si/Ni contact is surrounded by a region of greater barrier height ϕ_b^0. **b**, With $\phi_b^{Ni} = 0.61$ V the pinch-off model indicates a surrounding barrier of 0.82 and 0.91 V for the nonactivated and activated interfaces, respectively. The surrounding barrier height (ϕ_b^0) is the only fitting parameter. **c**, The conduction-band energy (E_{CB}) is plotted at V_{oc} under 1-sun illumination for a 60-nm-radius island with $\phi_b^0 = 0.91$. The inset shows a cross-section of the barrier through the centre of the island (radial distance = 0 nm) and at the edge of the island (radial distance = 60 nm). A pinched-off saddle point occurs with an effective barrier near 0.8 V—a value significantly greater than the average 0.61-V barrier height measured ex situ. **d**, The macroscopic voltammetry is consistent with that predicted by the pinch-off model. The photoelectrochemical data for n-Si with a 5-s Ni deposition are consistent with $\phi_b^0 = 0.91$ V, assuming uniform islands of 60-nm radius covering 15% of the surface. j_{cat}^0 is the catalyst exchange current density.

of its surroundings). For the system studied here, electron current decreases as Ni contacts become smaller, resulting in an increased photovoltage due to reduced recombination. This model has been invoked to explain low-temperature deviations from ideal Schottky-junction transport models[6], and used to control contact selectivity in nanowire devices by using high-/low-work-function layers acting as a surface gate[26]. In electrochemistry, the pinch-off effect has been used to explain the macroscopic behaviour of intentionally patterned semiconductor photoelectrodes;[20,25] the effect, however, has never been studied by examination of individual pinched-off nanocontacts.

We fit the experimental size-dependent photovoltage data to an analytical pinch-off model with a circular patch geometry (see Fig. 3a for model schematic and Supplementary Section 4 for additional discussion)[7,21,22]. The expression for the current through the nanocontact (I_{patch}) is given by the modified ideal-diode equation

$$I_{patch} = A^* T^2 C_a \left(e^{-\frac{q\phi_b^0}{kT} + C_b} \right) \left(e^{\frac{qV_{app}}{nkT}} - 1 \right) \quad (1)$$

where q is the elementary charge, V_{app} is the applied potential, k is the Boltzmann constant, T is the temperature, n is the ideality factor, C_a represents the effective contact area and C_b represents a decrease in the barrier height relative to the background barrier ϕ_b^0. The exact forms of C_a and C_b are dependent on the dopant density (N_D), band bending (V_{bb}), nanocontact radius (r) and Δ, the difference between ϕ_b^{Ni} and ϕ_b^0:

$$C_a = \frac{4\pi kT}{9q} \left(\frac{3\Delta r^2}{4} \right)^{1/3} \left(\frac{\epsilon_s}{qN_D V_{bb}} \right)^{2/3} \quad (2)$$

$$C_b = \frac{q}{kT} \left(\frac{3q\Delta r^2 V_{bb} N_D}{4\epsilon_s} \right)^{1/3} \quad (3)$$

The photovoltage data were assessed by assuming a patch barrier height of $\phi_b^{Ni} = 0.61$ V (the average n-Si/Ni contact barrier height) and then fitting the background barrier (ϕ_b^0) to the analytical model to reproduce the contact size dependence (Supplementary Section 4). The fits indicate $\phi_b^0 = 0.82$ V for the n-Si/Ni sample before intentional activation and $\phi_b^0 = 0.91$ V after photoelectrochemical activation (Fig. 3b). The chemical nature of this high-barrier region and the feasibility of the extracted ϕ_b^0 values are discussed in the subsequent section.

Pinch-off increases selectivity by reducing the flow of majority carriers that lead to recombination in the contact. Significant pinch-off behaviour is expected when $\frac{\Delta}{V_{bb}} > \frac{2r}{W}$, where W is the depletion-region thickness[30]. For ϕ_b^0 of 0.82 and 0.91 V with $\phi_b^{Ni} = 0.61$ V, significant pinch-off is predicted for contacts with radius below ~110 and 140 nm, respectively. The Ni particles studied

here have radii between 30 and 150 nm. To illustrate the effect of pinch-off on majority-carrier electron current, we plot the calculated conduction-band potential (E_{CB}) profile as a function of both the distance from the centre of a 60-nm-radius Ni nanocontact and the depth into the semiconductor (Fig. 3c). The junction is shown poised at open circuit under 1-sun illumination (corresponding to photoelectrochemical conditions where the back contact of the semiconductor is held at a potential near the photocurrent onset). A pinched-off 'saddle point' in the conduction-band energy with a maximum value near 0.8 V and a confined cross-section relative to the 120-nm Ni-particle diameter (Fig. 3b) is apparent. This increased barrier (relative to the macroscopic barrier of 0.61 V) results in a lower electron current and hence improved selectivity and reduced recombination. The pinch-off effect thus leads to photovoltages that are dependent not only on the contact's work function, but also its size, its geometry and the work function of the surrounding medium.

The pinch-off model can explain the observed current-potential data for the n-Si/Ni oxygen-evolving photoanodes (Fig. 1a). The experimental data are modelled by solving current continuity for the modified diode expression in series with a circuit element representing the catalyst driving the OER. The OER potential drop is obtained from a Butler–Volmer expression based on the measured OER activity of Ni electrodeposited on Pt (see Supplementary Section 4). The model is consistent with the experimental data for electrodes with 5-s deposition when the diode expression represents uniform Ni catalyst nanocontacts of radius 60 nm and 15% surface coverage (we observed 10–20% experimentally). These results suggest that, at least near the onset, the photocurrent is primarily passed through surface islands smaller than the average (radius 80 ± 25 nm) that have larger effective barrier heights. This model illustrates that the photocurrent-onset potential shift observed for small particles is completely accounted for by enhanced selectivity due to the pinch-off effect. The 60-s deposition produces Ni particles too large to leverage pinch-off and thus the photoelectrode response in that case is consistent with the bulk n-Si/Ni Schottky junction driving charge separation (Fig. 3d).

Chemical identity of the high-barrier region

Although the model shows that the photovoltage trend with nanocontact size can be explained by pinch-off, this requires the presence of a high-barrier region surrounding the n-Si/Ni contact. Since the experimentally measured dry barrier heights and illuminated V_{oc} values are independent of Ni nanocontact size (Fig. 2a,b), such a region is not present before photoelectrochemical activation. The activation process results in oxidation of any exposed Si to SiO_x and converts a portion of Ni to $Ni(OH)_2$/NiOOH. To evaluate the barrier height in surface regions covered only by the SiO_x layer (and not NiOOH or Ni), we performed Mott–Schottky impedance analysis in a ferro/ferricyanide electrolyte (aqueous 1 M KCl, 0.05 M $K_3Fe(CN)_6$ and 0.35 M $K_4Fe(CN)_6$) on bare n-Si photoanodes. The ferro/ferricyanide solution potential sets the barrier height at the n-Si/electrolyte interface to ~0.7 V (larger than the n-Si/Ni barrier height of ~0.6 V). Anodic cycling of n-Si leads to the growth of a SiO_x passivation layer. Subsequent Mott–Schottky analysis shows that the SiO_x layer lowers the barrier height to ~0.5 V (Supplementary Section 5). This indicates that SiO_x cannot be responsible for setting the proposed large background barrier height around the Ni islands.

Another possible mechanism is that oxidized catalyst with a large work function induces the large background barrier. To evaluate the barrier height of $Ni(OH)_2$/NiOOH on n-Si, we fabricated dual-working-electrode devices by (1) depositing a 2-nm-thick uniform Ni metal layer on n-Si via electron-beam evaporation; (2) photodepositing additional Ni (oxy)hydroxide from saturated $NiCl_2$ solution in 1 M aqueous K-borate buffer (pH 9.5) by applying 0.625 V versus $\mathcal{E}_{O_2/OH^-}$ under 1-sun illumination for 30 s; (3) photoelectrochemically cycling the electrode in 1 M K-borate buffer until no photocurrent was evident (which oxidized remaining Ni metal and the n-Si surface); and (4) depositing a 10-nm-thick porous Au contact layer on the catalyst surface (Fig. 4a and Supplementary Section 6). The Au contact on these metal-oxide-semiconductor-type devices was biased, in an electrochemical cell, to hold the catalyst layer in either its reduced $Ni(OH)_2$ or oxidized (NiOOH) form while impedance spectroscopy was performed at a series of fixed biases between the Au and back-semiconductor contacts (Fig. 4b). Mott–Schottky[23] analysis of the extracted bias-dependent depletion capacitances yielded dopant densities consistent with the manufacturer's specifications ($5–8 \times 10^{15}$ cm^{-3}) and show that the interfacial barrier is dependent on the redox state of the catalyst (Fig. 4b, inset). When the Au top contact is poised to hold the catalyst in the $Ni(OH)_2$ state, the barrier height is 0.65 V; when the catalyst is oxidized (that is, in the OER-active state), the barrier is 1.04 V, similar to the large background barrier heights indicated by the fit to the analytical pinch-off model (Fig. 3b). Figure 4c–e depicts the band-bending and barrier-height differences between Ni, $Ni(OH)_2$ and NiOOH contacts, respectively, to n-Si. This result is conceptually similar to so-called 'adaptive junctions', where the barrier height of a contact to an *n*-type semiconductor is enhanced during operation as an electrolyte-permeable contact is converted to a higher oxidation state by accumulated holes[31,32]. It is also consistent with n-Si/Al_2O_3/Pt/Ni photoanodes where the barrier height was increased by 0.23 V following oxidation of the Ni catalyst, although it was noted that the thin Pt layer partially screened the effect[33].

The dual-working-electrode results are consistent with the hypothesis that n-Si/Ni photoanodes exhibit an emergent pinch-off phenomenon. After photoanodic generation of NiOOH, high-barrier regions on n-Si are produced because the work function of NiOOH (>5.3 eV)[34] is larger than that of metallic Ni (5.0 eV). This large barrier is also consistent with the $Ni(OH)_2$/NiOOH redox potential (~1.35 V versus the reversible hydrogen electrode) being >1 V more positive than the flat-band potential of n-Si (~0.25 V versus the reversible hydrogen electrode)[35]. The improved photocurrent-onset potentials for activated devices with smaller Ni particles (5-s deposition) are therefore due to low-barrier n-Si/Ni interfaces pinched-off by high-barrier n-Si/SiO_x/NiOOH interfaces (Fig. 5). The pinched-off n-Si/Ni junctions form selective contacts and suppress majority-carrier electron transfer to the catalyst, compared to nonpinched-off analogues, while maintaining direct, low-resistance electrical connection between the Ni and n-Si. Photoanodes decorated with large islands (for example, radius >140 nm), or those that have not been activated to form the NiOOH layer (Supplementary Fig. 7), show poor performance due to the absence of this pinch-off phenomenon improving Ni nanocontact selectivity. Continued activation (beyond 50 cycles) further improves the photocurrent onset until the underlying n-Si is oxidized when the Ni is completely converted to electrolyte-permeable NiOOH, blocking all current flow (Supplementary Section 7). The improvement is attributed to increased Ni oxidation, which enhances pinch-off by decreasing the n-Si/Ni contact area. The extent of NiOOH necessary to produce pinch-off is discussed in Supplementary Section 8 and is supported by COMSOL finite-element simulations of the nanoscale junction.

To further test the pinch-off hypothesis, we deposited Ni for 5 s, oxidized the Si and Ni surfaces via 50 photoelectrochemical potential cycles, deposited Ni for an additional 5 s, repeated the photoelectrochemical potential cycling, and then electroplated Ni for an additional 50 s (Fig. 5b). The devices formed with this progressive deposition showed a photocurrent-onset potential ~250 mV more positive than n-Si/Ni devices fabricated with continuous 60-s Ni electrodeposition (Supplementary Section 9). The light-limited photocurrent and integrated redox peaks for the progressive samples, however, are similar to the continous samples indicating a

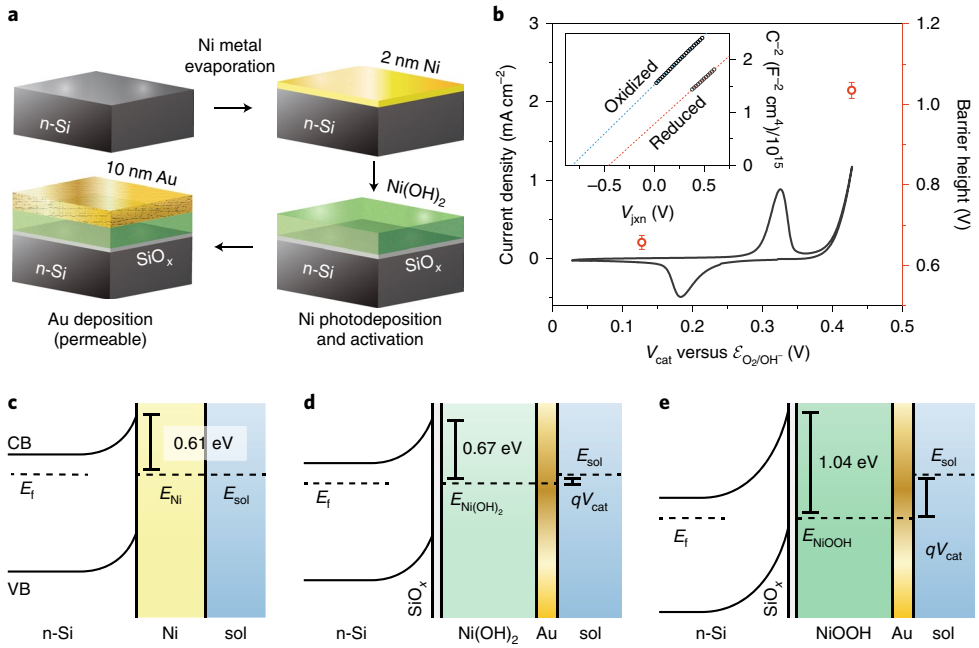

Fig. 4 | Dual-working-electrode device measurement shows that high-barrier contacts are formed from oxidized NiOOH during operation. a, The schematic illustrates how dual-working-electrode devices are fabricated. Connections to the rear of n-Si and to the Au layer are used to perform impedance experiments, while the $Ni(OH)_2$/NiOOH layer is potentiostatically held in either it's reduced (V_{cat} = 0.125 V versus $\mathcal{E}_{O_2/OH^-}$) or oxidized (V_{cat} = 0.425 V versus $\mathcal{E}_{O_2/OH^-}$) state. **b**, The voltammograms show $Ni(OH)_2$/NiOOH redox behaviour as it is cycled through the Au secondary working electrode at 20 mV s^{-1} in 1 M aqueous K-borate buffer at pH 9.5. V_{cat} is the potential applied to the catalyst layer via the top porous Au contact. Mott–Schottky analysis on the impedance data collected between the Au and semiconductor rear contact (inset) shows that oxidation of $Ni(OH)_2$ to NiOOH caused the barrier height to increase from 0.66 to 1.04 V. **c**–**e**, Band-bending diagrams, as deduced from Mott–Schottky analysis, are shown for metallic Ni (**c**), $Ni(OH)_2$ (**d**) and NiOOH (**e**) contacts to n-Si. Barrier height increases as the Ni is successively oxidized to higher oxidation states. E_f, E_{Ni}, $E_{Ni(OH)_2}$, E_{NiOOH} and E_{sol} represent the electrochemical potential for the semiconductor, Ni, $Ni(OH)_2$, NiOOH and solution ($E_{sol} = q\,\mathcal{E}_{O_2/OH^-}$), respectively. CB and VB represent the semiconductor conduction and valence band, respectively. The magnitude of qV_{cat} is depicted in **d** and **e** and corresponds to the data points in **b**. See Supplementary Section 6 for further discussion.

comparable Ni surface area. These results are explained by the fact that the potential-cycling step oxidizes the underlying Si surface in regions where Ni has not been deposited, and subsequent Ni deposition serves only to grow the existing Ni nanoparticles without increasing the n-Si/Ni contact area. The pinched-off junction is thus maintained.

Pinch-off in photoelectrode devices

Our direct measurements of pinch-off help explain previous observations for a variety of catalyst-coated semiconductor photoelectrodes. It was found that 2-nm-thick Ni layers on n-Si show a photocurrent onset 200 mV more negative than 5-nm-thick layers[18]. This difference cannot be explained by resistive losses through the thicker catalyst layer or parasitic light loss[5]. These data are readily explained, however, by electrochemical activation of the 2-nm Ni film that produced nanoscale low-barrier semiconductor/metal contacts pinched-off by high-barrier semiconductor/oxide/metal-oxyhydroxide contacts[5]. Similar observations have been noted for devices where catalyst nanocontacts were intentionally deposited. It was noted that a ~200-mV improvement in photocurrent-onset potential resulted after 40 photoelectrochemical conditioning cycles for n-Si coated with Ni nanoislands (59 ± 17 nm diameter) compared to n-Si coated with a uniform Ni film[17]. A similar improvement in photocurrent onset was found, without activation, when NiOOH was photodeposited after initial Ni metal island formation[36]. Annealing the Ni metal nanoparticles to oxidize their surface has also been shown to improve photocurrent onset without the requirement for electrochemical cycling[37]. For n-Si/Co photoanodes, the barrier height was found to be a function of Co coverage with low coverage (that is, coalesced islands of diameter 21 ± 8 nm) yielding photoanodes with a 360-mV improvement in photocurrent onset relative to uniform Co films (pinch-off was also hypothesized and rationalized in this work, but not analysed via direct measurement)[23]. For p-GaAs photocathodes, better hydrogen evolution performance was achieved using small Pt nanoparticles 10 nm in diameter relative to 90-nm particles[38]. p-Si nanowires decorated with $NiCoSe_x$ nanoparticles showed a 110-mV improvement in flat-band potential relative to a planar $NiCoSe_x$/p-Si[39]. For particulate semiconductors, size-dependent photocatalytic activity has been observed for particulate n-TiO_2 decorated with Au nanoparticles, with the smallest nanoparticles being the most active[40]. The above results are probably due to pinch-off where the high-barrier region is attributed to contact with either oxidized catalyst or the electrolyte.

The insight illustrated here may be useful in designing improved devices by engineering nanocontact selectivity. Although high-performance selective contacts to Si can be achieved by forming doped-semiconductor homo-/heterojunctions[41], for some applications carrier-selective junctions formed by the deposition of electrochemically stable contacts may be useful[42]. This approach is difficult, however, because of the lack of materials that form carrier-selective heterojunctions while also remaining stable and electrically conductive under electrochemical conditions. An alternative strategy might focus on the deposition of stable/conductive nanocontacts before engineering the surrounding surface to induce selectivity via pinch-off (see Supplementary Section 9). For emerging

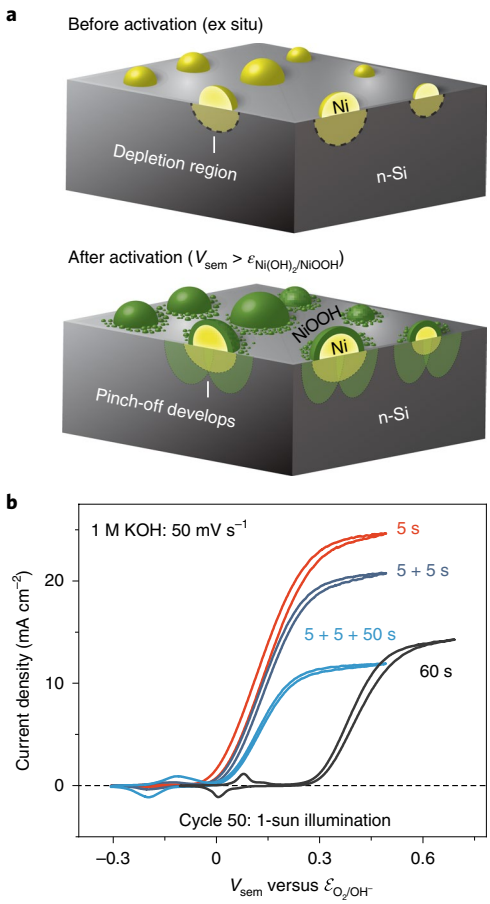

Fig. 5 | n-Si/Ni nanocontacts produce a pinched-off junction following activation. a, Schematic illustrating the depletion regions produced by the surface contacts before and after activation. Although the initial depletion region is small, the conversion of surface Ni to NiOOH produces a larger depletion region that results in the n-Si/Ni contact being pinched-off and an increase in selectivity. The necessary extent of conversion required to produce pinch-off is discussed in Supplementary Section 8. Simulations show that NiOOH probably extends on the surface beyond the clearly evident shell, consistent with experimental observations of the surface after electrochemical conditioning and as illustrated in the lower panel. **b**, The pinch-off hypothesis is corroborated by examination of devices with cumulative 60-s electrodeposition where the pinched-off junction is intentionally retained. By halting electrodeposition after 5 and 10 s to perform activation cycles that generate an interfacial SiO_x, the photocurrent onset remains near that of devices with 5-s Ni electrodeposition.

photoelectrode materials, particularly oxides[1] such as $BiVO_4$ or photoactive particulate semiconductors like TiO_2 and $SrTiO_3$ (refs. [43,44]), designing carrier-selective contacts is even more difficult. This challenge might be addressed by using sufficiently small catalytic contacts and engineering the surrounding surface (which does not need to provide catalytic sites or collect charge) to induce a large interface electrostatic barrier. The redox activity of such a selectivity-inducing material might be leveraged to improve selectivity during operation.

Nanoscale potential sensing

Understanding and controlling the selective flow of electrons and holes is critical in the design of efficient photoelectrochemical devices. We provide an example of spatially resolved potential measurements on electronically isolated nanoscale features in operating photoelectrochemical systems. This capability enables direct interrogation of the interfacial behaviour of nanoscale contacts with semiconductor photoelectrodes. By translating this approach to polycrystalline thin-film[11] or nanostructured[45] photoelectrodes coated with nanoparticle catalysts, heterogeneity in the underlying semiconductor properties could be probed through their effect on the photovoltage measured at individual nanoparticle semiconductor/catalyst contacts. This technique should further enable studies of catalyst-contact properties in particulate photoelectrochemical systems where both anode and cathode catalyst are dispersed on the same semiconductor particle[44,46]. We show that PS-EC-AFM enables nanoscale measurements of pinch-off at individual nanocontacts. For photoelectrochemical devices, the pinch-off effect was previously experimentally studied only via macroscopic current–voltage measurements using intentionally nanofabricated monodisperse contacts and a reversible redox couple[25]. The pinch-off phenomena studied here provide evidence that the effect can be used, possibly in a wide range of semiconductor and catalyst systems, to create photoelectrochemical devices of high efficiency.

The ability to measure local surface potentials with PS-EC-AFM could be useful in other areas. The technique and data interpretation are straightforward, with measurements reliant only on electrochemical potential equilibration between the AFM tip and the feature of interest. Nanoscale-resolved surface-potential sensing is perhaps useful in measuring the heterogeneity of processes in fuel-cell/electrolyser catalyst–ionomer structures[47] and intercalation/de-intercalation phenomena in battery electrodes[48]. The technique might aid in biological research, where potential measurement of physiologically relevant electrolytes is challenging[10,49], by allowing, with appropriate electrode architectures, local measures of bacterial[49] and membrane surface potentials[50]. The technique could also be adapted to apply potential to nanoscale features rather than sensing potential. It may be possible to locally study charge-transfer processes and extract basic parameters related to conductivity, catalytic rates and double-layer capacitance on isolated nanoscale features in operating (photo)electrochemical systems.

Online content

Any methods, additional references, Nature Research reporting summaries, source data, statements of code and data availability and associated accession codes are available at https://doi.org/10.1038/s41563-019-0488-z.

Received: 22 May 2019; Accepted: 18 August 2019;
Published online: 7 October 2019

References

1. Sivula, K. & van de Krol, R. Semiconducting materials for photoelectrochemical energy conversion. *Nat. Rev. Mater.* **1**, 15010 (2016).
2. Chen, R. T., Fan, F. T., Dittrich, T. & Li, C. Imaging photogenerated charge carriers on surfaces and interfaces of photocatalysts with surface photovoltage microscopy. *Chem. Soc. Rev.* **47**, 8238–8262 (2018).
3. Mei, B., Han, K. & Mul, G. D. Driving surface redox reactions in heterogeneous photocatalysis: the active state of illuminated semiconductor-supported nanoparticles during overall water-splitting. *ACS Catal.* **8**, 9154–9164 (2018).
4. Laskowski, F. A. L., Nellist, M. R., Qu, J. J. & Boettcher, S. W. Metal oxide/(oxy)hydroxide overlayers as hole collectors and oxygen-evolution catalysts on water-splitting photoanodes. *J. Am. Chem. Soc.* **141**, 1394–1405 (2019).
5. Laskowski, F. A. L., Nellist, M. R., Venkatkarthick, R. & Boettcher, S. W. Junction behavior of n-Si photoanodes protected by thin Ni elucidated from dual working electrode photoelectrochemistry. *Energy Environ. Sci.* **10**, 570–579 (2017).
6. Tung, R. T. The physics and chemistry of the Schottky barrier height. *Appl. Phys. Rev.* **1**, 011304 (2014).
7. Tung, R. T. Electron-transport of inhomogeneous Schottky barriers. *Appl. Phys. Lett.* **58**, 2821–2823 (1991).
8. Tennyson, E. M., Gong, C. & Leite, M. S. Imaging energy harvesting and storage systems at the nanoscale. *ACS Energy Lett.* **2**, 2761–2777 (2017).

9. Collins, L. et al. Probing charge screening dynamics and electrochemical processes at the solid-liquid interface with electrochemical force microscopy. *Nat. Commun.* **5**, 3871 (2014).
10. Collins, L., Kilpatrick, J. I., Kalinin, S. V. & Rodriguez, B. J. Towards nanoscale electrical measurements in liquid by advanced KPFM techniques: a review. *Rep. Prog. Phys.* **81**, 086101 (2018).
11. Eichhorn, J. et al. Nanoscale imaging of charge carrier transport in water splitting photoanodes. *Nat. Commun.* **9**, 2597 (2018).
12. Esposito, D. V., Levin, I., Moffat, T. P. & Talin, A. A. H_2 evolution at Si-based metal-insulator-semiconductor photoelectrodes enhanced by inversion channel charge collection and H spillover. *Nat. Mater.* **12**, 562–568 (2013).
13. Mariano, R. G., McKelvey, K., White, H. S. & Kanan, M. W. Selective increase in CO_2 electroreduction activity at grain-boundary surface terminations. *Science* **358**, 1187–1191 (2017).
14. Hurth, C., Li, C. Z. & Bard, A. J. Direct probing of electrical double layers by scanning electrochemical potential microscopy. *J. Phys. Chem. C* **111**, 4620–4627 (2007).
15. Yoon, Y. H., Woo, D. H., Shin, T., Chung, T. D. & Kang, H. Real-space investigation of electrical double layers. Potential gradient measurement with a nanometer potential probe. *J. Phys. Chem. C* **115**, 17384–17391 (2011).
16. Nellist, M. R. et al. Potential-sensing electrochemical atomic force microscopy for in operando analysis of water-splitting catalysts and interfaces. *Nat. Energy* **3**, 46–52 (2018).
17. Loget, G., Fabre, B., Fryars, S., Meriadec, C. & Ababou-Girard, S. Dispersed Ni nanoparticles stabilize silicon photoanodes for efficient and inexpensive sunlight-assisted water oxidation. *ACS Energy Lett.* **2**, 569–573 (2017).
18. Kenney, M. J. et al. High-performance silicon photoanodes passivated with ultrathin nickel films for water oxidation. *Science* **342**, 836–840 (2013).
19. Oh, K. et al. Elucidating the performance and unexpected stability of partially coated water-splitting silicon photoanodes. *Energy Environ. Sci.* **11**, 2590–2599 (2018).
20. Loget, G. Water oxidation with inhomogeneous metal-silicon interfaces. *Curr. Opin. Colloid Interface Sci.* **39**, 40–50 (2019).
21. Sullivan, J. P., Tung, R. T., Pinto, M. R. & Graham, W. R. Electron-transport of inhomogeneous Schottky barriers - a numerical study. *J. Appl. Phys.* **70**, 7403–7424 (1991).
22. Tung, R. T. Electron-transport at metal-semiconductor interfaces - general theory. *Phys. Rev. B* **45**, 13509–13523 (1992).
23. Hill, J. C., Landers, A. T. & Switzer, J. A. An electrodeposited inhomogeneous metal-insulator-semiconductor junction for efficient photoelectrochemical water oxidation. *Nat. Mater.* **14**, 1150–1155 (2015).
24. Roe, E. T., Egelhofer, K. E. & Lonergan, M. C. Limits of contact selectivity/recombination on the open-circuit voltage of a photovoltaic. *ACS. Appl. Energy. Mater.* **1**, 1037–1046 (2018).
25. Rossi, R. C., Tan, M. X. & Lewis, N. S. Size-dependent electrical behavior of spatially inhomogeneous barrier height regions on silicon. *Appl. Phys. Lett.* **77**, 2698–2700 (2000).
26. Oener, S. Z. et al. Charge carrier-selective contacts for nanowire solar cells. *Nat. Commun.* **9**, 3248 (2018).
27. Burke, M. S., Enman, L. J., Batchellor, A. S., Zou, S. H. & Boettcher, S. W. Oxygen evolution reaction electrocatalysis on transition metal oxides and (oxy)hydroxides: activity trends and design principles. *Chem. Mater.* **27**, 7549–7558 (2015).
28. Li, S. Y. et al. Enhancing the photovoltage of Ni/n-Si photoanode for water oxidation through a rapid thermal process. *ACS Appl. Mater. Interfaces* **10**, 8594–8598 (2018).
29. Nellist, M. R. et al. Atomic force microscopy with nanoelectrode tips for high resolution electrochemical, nanoadhesion and nanoelectrical imaging. *Nanotechnology* **28**, 095711 (2017).
30. Tung, R. T. Recent advances in Schottky barrier concepts. *Mater. Sci. Eng. R Rep.* **35**, 1–138 (2001).
31. Lin, F. D. & Boettcher, S. W. Adaptive semiconductor/electrocatalyst junctions in water-splitting photoanodes. *Nat. Mater.* **13**, 81–86 (2014).
32. Nellist, M. R., Laskowski, F. A. L., Lin, F. D., Mills, T. J. & Boettcher, S. W. Semiconductor-electrocatalyst interfaces: theory, experiment, and applications in photoelectrochemical water splitting. *Acc. Chem. Res.* **49**, 733–740 (2016).
33. Digdaya, I. A., Adhyaksa, G. W. P., Trzesniewski, B. J., Garnett, E. C. & Smith, W. A. Interfacial engineering of metal-insulator-semiconductor junctions for efficient and stable photoelectrochemical water oxidation. *Nat. Commun.* **8**, 15968 (2017).
34. Ratcliff, E. L. et al. Evidence for near-surface NiOOH species in solution-processed NiO_x selective interlayer materials: impact on energetics and the performance of polymer bulk heterojunction photovoltaics. *Chem. Mater.* **23**, 4988–5000 (2011).
35. Röppischer, H., Bumai, Y. A. & Feldmann, B. Flatband potential studies at the n-Si/electrolyte interface by electroreflectance and C-V measurements. *J. Electrochem. Soc.* **142**, 650–655 (1995).
36. Xu, G. Z. et al. Silicon photoanodes partially covered by $Ni@Ni(OH)_2$ core-shell particles for photoelectrochemical water oxidation. *ChemSusChem* **10**, 2897–2903 (2017).
37. Lee, S. A. et al. Tailored NiO_x/Ni cocatalysts on silicon for highly efficient water splitting photoanodes via pulsed electrodeposition. *ACS Catal.* **8**, 7261–7269 (2018).
38. Choi, K., Kim, K., Moon, I. K., Oh, I. & Oh, J. Evaluation of electroless Pt deposition and electron beam Pt evaporation on p-GaAs as a photocathode for hydrogen evolution. *ACS. Appl. Energy Mater.* **2**, 770–776 (2019).
39. Zhang, H. X. et al. A p-Si/$NiCoSe_x$ core/shell nanopillar array photocathode for enhanced photoelectrochemical hydrogen production. *Energy Environ. Sci.* **9**, 3113–3119 (2016).
40. Wang, N., Tachikawa, T. & Majima, T. Single-molecule, single-particle observation of size-dependent photocatalytic activity in Au/TiO_2 nanocomposites. *Chem. Sci.* **2**, 891–900 (2011).
41. Yoshikawa, K. et al. Silicon heterojunction solar cell with interdigitated back contacts for a photoconversion efficiency over 26%. *Nat. Energy* **2**, 17032 (2017).
42. Hu, S. et al. Thin-film materials for the protection of semiconducting photoelectrodes in solar-fuel generators. *J. Phys. Chem. C* **119**, 24201–24228 (2015).
43. Takata, T. & Domen, K. Particulate photocatalysts for water splitting: recent advances and future prospects. *ACS Energy Lett.* **4**, 542–549 (2019).
44. Wang, Q. et al. Scalable water splitting on particulate photocatalyst sheets with a solar-to-hydrogen energy conversion efficiency exceeding 1%. *Nat. Mater.* **15**, 611–615 (2016).
45. Su, Y. D. et al. Single-nanowire photoelectrochemistry. *Nat. Nanotechnol.* **11**, 609–612 (2016).
46. Wang, J., Zhao, J. & Osterloh, F. E. Photochemical charge transfer observed in nanoscale hydrogen evolving photocatalysts using surface photovoltage spectroscopy. *Energy Environ. Sci.* **8**, 2970–2976 (2015).
47. Litster, S. & McLean, G. PEM fuel cell electrodes. *J. Power Sources* **130**, 61–76 (2004).
48. Takahashi, Y. et al. Nanoscale visualization of redox activity at lithium-ion battery cathodes. *Nat. Commun.* **5**, 5420 (2014).
49. Marliere, C. & Dhahri, S. An in vivo study of electrical charge distribution on the bacterial cell wall by atomic force microscopy in vibrating force mode. *Nanoscale* **7**, 8843–8857 (2015).
50. Pfreundschuh, M., Hensen, U. & Muller, D. J. Quantitative imaging of the electrostatic field and potential generated by a transmembrane protein pore at subnanometer resolution. *Nano Lett.* **13**, 5585–5593 (2013).

Acknowledgements

This work was funded by the Department of Energy, Basic Energy Sciences (award no. DE-SC0014279). F.A.L.L. acknowledges support from a NSF graduate research fellowship (no. 1309047). S.Z.O. acknowledges support from a research fellowship of the German Research Foundation (Deutsche Forschungsgemeinschaft, under project no. 408246589 (OE 710/1-1)). The atomic force microscope was purchased using funds provided by the NSF Major Research Instrumentation Program (grant no. DMR-1532225). We acknowledge use of shared instrumentation in the Center for Advanced Materials Characterization in Oregon and Rapid Materials Prototyping facilities, which are supported by grants from the M.J. Murdock Charitable Trust, the W.M. Keck Foundation, Oregon Nanoscience and Microtechnologies Institute and the National Science Foundation.

Author contributions

F.A.L.L. and S.W.B. conceived the experiments and led the project. F.A.L.L. conducted the analytical modelling/coding and the dual-working-electrode experiments. F.A.L.L. and M.R.N. performed the operando photoelectrochemical experiments. F.A.L.L., A.M.G., D.C.B. and J.L.F. prepared photoelectrodes and conducted the ex situ AFM experiments. S.Z.O. was responsible for cross-sectional scanning electron microscope (SEM) analysis and contributed significantly to analysis of diode properties from conductive AFM data. F.A.L.L. and S.W.B. wrote the manuscript with input from all authors.

Competing interests

The authors declare no competing interests.

Additional information

Supplementary information is available for this paper at https://doi.org/10.1038/s41563-019-0488-z.

Correspondence and requests for materials should be addressed to S.W.B.

Reprints and permissions information is available at www.nature.com/reprints.

Publisher's note Springer Nature remains neutral with regard to jurisdictional claims in published maps and institutional affiliations.

© The Author(s), under exclusive licence to Springer Nature Limited 2019

Methods

Photoanode fabrication. Procedures for the fabrication of n-Si photoanodes with Ni nanocontacts were adapted from ref. [17]. Phosphorus-doped n-Si [100] wafers (0.65–0.95 Ω cm, University Wafer) were diced into $1 \times 1\ cm^2$ squares and sequentially sonicated for 10 min each in acetone, isopropyl alcohol and water (18.2 MΩ cm). The n-Si squares were placed in boiling piranha (~100 °C, 3/1 by volume concentrated aqueous H_2SO_4/30% aqueous H_2O_2, both from Fisher Chemical) for 30 min and then vigorously rinsed with water (18.2 MΩ cm) before drying under N_2. An ohmic contact was established to the rear of each n-Si square by applying Ga-In eutectic (≥99.99%, Sigma Aldrich), scratching within the Ga-In with a diamond scribe to ensure contact and then affixing one end of a Sn–Cu wire (length ~25 cm, –30 American wire gauge, McMaster Carr) within the eutectic using hot glue (SureBonder Mini). The Sn–Cu wire was fed through a glass tube (diameter 7 mm) and constructed into an electrode suitable for side-illumination with the n-Si rear and adjacent Sn–Cu wire insulated by hot glue. The Ni electrodeposition solution (aqueous 0.01 M $NiCl_2$ + 0.1 M H_3BO_3) was produced fresh for each batch of electrodes, by dissolving $NiCl_2 \cdot 6H_2O$ (99.9%, Sigma Aldrich) and H_3BO_3 (≥99.5%, Sigma Aldrich) in water (18.2 MΩ cm) and sonicating until dissolution was complete (typically 10 min). Immediately before deposition, electrodes were submerged in a buffered HF etching solution (20/1 buffered oxide etch, J.T. Baker) for 2 min and then rinsed with water (18.2 MΩ cm). For deposition of the Ni islands, the electrode, a Pt wire coil serving as a counter-electrode and a commercial Ag/AgCl reference electrode (BASi MF-2052) were placed in the $NiCl_2$-based deposition solution and −1.5 V versus Ag/AgCl was applied for 5, 15 or 60 s using a Bio-Logic SP200 potentiostat (see Supplementary Section 1).

Photoelectrochemical characterization. The photoelectrochemical behaviour of photoanodes was tested in both aqueous 1 M KOH and a 1 M potassium borate buffer (K-borate) adjusted to pH 9.5. Characterization was conducted in 1 M KOH to illustrate the photoelectrochemical activity in an environment where oxygen-evolution catalysis is facile. However, 1 M K-borate buffer was selected for operando studies with PS-EC-AFM to decrease any etching of the Si surface that might occur between initial topographical characterization and photovoltage measurement, as well as to preserve the longevity of the EC-AFM tips. For photoelectrode characterization, the electrodes were activated via 50 voltammogram cycles in either electrolyte solution under 100 mW cm^{-2} of solar simulation (Abet Technologies, 10500) using the Ag/AgCl reference and Pt counter electrodes. The activation potential range varied based on Ni deposition time, but was always conducted at 50 mV s^{-1} with one endpoint cathodic of the catalyst's reduction peak, nominally $NiOOH + e^- + H_2O \rightarrow Ni(OH)_2 + OH^-$, and the other endpoint positioned in the light-limited photocurrent range. Photocurrent-onset potentials (versus $\mathcal{E}_{O_2/OH^-}$) and the magnitude of the light-limiting photocurrent were comparable for electrodes with the same electrodeposition time, irrespective of the electrolyte solution. Photocurrent-onset slopes were steeper when electrodes were measured in the 1 M KOH solution, consistent with higher OER activity and electrolyte conductivity relative to measurements in the buffered solution.

Potential-sensing AFM. Operando potential sensing was performed using commercial PeakForce SECM probes on a custom-modified Bruker Dimensional Icon AFM. Photoelectrodes were dissected, immediately following Ni electrodeposition, using a razor blade to remove hot-glue insulation. A custom cell was designed where the dissected n-Si square chip was affixed to a Kel-F baseplate featuring a hole to accommodate the ohmic back contact. Epoxy (Hysol Loctite 9460) was used to affix the photoanode and insulate the ohmic contact from the electrolyte. A groove was machined around the photoanode mounting area, which accommodated a Pt-coil counter-electrode and a standard Ag/AgCl reference electrode (Pine Research). During experiments the cell was filled with aqueous 1 M K-borate (pH 9.5) such that the photoanode was covered by at least 1 mm of solution. A Bio-Logic SP300 potentiostat was used, with the working electrode connection attached to the photoanode's ohmic contact and the counter-electrode potential-sensing lead attached to the rear of the PeakForce SECM probe (through a strain-release module) to monitor the tip potential. The built-in AFM laser (power, 1 mW; illumination area, $\sim 8 \times 10^{-4}\ cm^2$; wavelength, 690 nm), which tracks with the AFM tip, was used as a local illumination source. The surface was then imaged in PeakForce Tapping mode to identify areas suitable for photovoltage measurement (ideally where most Ni nanoparticles could be well resolved from adjacent particles). After identification of a suitable area, bias was applied to the photoanode to oxidize the $Ni(OH)_2$ shell while simultaneously producing no bubbles. This was accomplished by setting either a chronoamperometry condition (typically $V_{sem} = 0.7$ V versus Ag/AgCl) or chronopotentiometry condition (typically $I = 1\ \mu A$). Once a stable bias was maintained, islands were contacted using the Bruker software's point-and-shoot function and the surface potential was recorded.

Data availability

The data that support the findings of this study are available from the corresponding author upon reasonable request.

Code availability

Code used for the pinch-off simulations can be downloaded as a Supplementary Information file.